GEOPHYSICS, VOL. 66, NO. 1 (JANUARY-FEBRUARY 2001); P. 158–173, 18 FIGS., 1 TABLE.

Multisite, multifrequency tensor decomposition of magnetotelluric data

Gary W. McNeice* and Alan G. Jones‡

ABSTRACT

Accurate interpretation of magnetotelluric data requires an understanding of the directionality and dimensionality inherent in the data, and valid implementation of an appropriate method for removing the effects of shallow, small-scale galvanic scatterers on the data to yield responses representative of regional-scale structures. The galvanic distortion analysis approach advocated by Groom and Bailey has become the most adopted method, rightly so given that the approach decomposes the magnetotelluric impedance tensor into determinable and indeterminable parts, and tests statistically the validity of the galvanic distortion assumption. As proposed by Groom and Bailey, one must determine the appropriate frequency-independent telluric distortion parameters and geoelectric strike by fitting the seven-parameter model on a frequency-by-frequency and site-by-site basis independently. Although this approach has the attraction that one gains a more intimate understanding of the data set, it is rather time-consuming and requires repetitive application. We propose an extension to Groom-Bailey decomposition in which a global minimum is sought to determine the most appropriate strike direction and telluric distortion parameters for a range of frequencies and a set of sites. Also, we show how an analytically-derived approximate Hessian of the objective function can reduce the required computing time. We illustrate application of the analysis to two synthetic data sets and to real data. Finally, we show how the analysis can be extended to cover the case of frequency-dependent distortion caused by the magnetic effects of the galvanic charges.

INTRODUCTION

During the 1990s, tensor decomposition analysis has become an integral part of the interpretation of magnetotelluric (MT) data for one-dimensional (1-D) and two-dimensional (2-D) regional structures (Eisel and Bahr, 1993; Harinarayana et al., 1993; Jones and Dumas, 1993; Jones et al., 1993a, b; Kurtz et al., 1993; Ogawa et al., 1994, 1996; Boerner et al., 1995; Gupta and Jones, 1995; Marquis et al., 1995; Livelybrooks et al., 1996; Chave and Jones, 1997; Constable et al., 1997; Echternacht et al., 1997; Kawakami et al., 1997; Ogawa, 1997; Pous et al., 1997; Toh et al., 1997; White et al., 1997, 1999; Adam, 1998; Ingham and Brown, 1998; Borner et al., 1999; Volti, 1999). The objective of this analysis is to remove the first-order effects of galvanic distortions produced by small-scale, near-surface inhomogeneities in conductivity, and to determine the impedances and strike of the regional 2-D geoelectric structure(s). Regional strike is often one of the poorest resolved of the parameters recovered during decomposition analysis (Groom et al., 1993; Jones and Groom, 1993), which presents a problem since the accuracy of the interpretation is highly dependent on its correct determination.

In addition to the problem of poor resolution, the inherent instability in the determination of regional strike in the presence of noise and galvanic distortion (Jones and Groom, 1993) leads to instability in decomposition procedures based on the rotation of the impedance tensor, such as those of Bahr (1988, 1991), Chakridi et al. (1992), Zhang et al. (1987) and Smith (1995, 1997). Superior estimates of distortion and regional MT parameters are obtained by fitting, in a least-squares sense, a parametric, physically-based model of distortion to the observed impedance tensor (Bailey and Groom, 1987; Groom and Bailey 1989, 1991; Groom et al., 1993), and the fit of the model tested statistically. The Groom-Bailey (GB) approach also differs in a significant manner from other distortion methods in that the effects of galvanic distortion are separated into determinable and indeterminable parts, whereas in other methods

Manuscript received by the Editor December 16, 1998; revised manuscript received February 22, 2000.
*Formerly at Memorial University of Newfoundland, Department of Earth Sciences, St. John's, Newfoundland A1B 3X5, Canada. Presently at Geosystem Canada, Inc., 927 Raftsman Lane, Ottawa, Ontario K1C 2V3, Canada. E-mail: gmcneice@geosystem.net.
‡Geological Survey of Canada, Continental Geoscience Division, 615 Booth Street, Room 218, Ottawa, Ontario K1A 0E9, Canada. E-mail: ajones@cg.NRCan.gc.ca.

these are inextricably linked in complex ways. Although this decomposition may not seem to be intuitive to some, it performs a critical component of distortion removal. In GB analysis, the determinable part of galvanic distortion is characterized by two galvanic distortion parameters, *shear* and *twist*, and induction by the *regional strike* and the *regional impedances*. The indeterminable quantities are amplitude shifts of the two regional impedances.

Usually, shear, twist, and strike are iteratively constrained to find frequency-independent estimates required by the decomposition model (see Groom et al., 1993, for a tutorial). The regional strike determined for each of a set of sites is then compared to obtain an estimate of regional strike for the entire data set (assuming the data are sensing the same regional 2-D structure). For a more representative estimate of regional strike, one really needs to perform a weighted average of the determined strike estimates, since the resolution of regional strike is a function of frequency, site location, and data precision.

In this paper, we briefly review the tenets of GB decomposition and propose an extension in which all the physical constraints implicit to the decomposition model are imposed simultaneously on the data set and a global minimum misfit solution sought. This procedure derives an estimate of regional strike that is most consistent with the data set in some statistical manner, and provides the interpreter with information on the degree to which the whole dataset, or data subset, fit the model of regional 2-D with galvanic 3-D distortions. Rather than derive the Hessian of the objective function numerically, we show that an analytically-derived approximate estimate leads to a more stable and robust solution with less computation. The determination of confidence intervals for the derived parameters is performed using a bootstrap approach.

Synthetic datasets and a real dataset from Papua New Guinea are used to demonstrate the proposed decomposition analysis. Extension to deal with frequency-dependent distortion caused by the magnetic effects of the galvanic charges is described, but its implementation is shown to be problematic. As with many model-fitting procedures, it is highly recommended that the user proceed with caution, as the extended decomposition can, and will, fail under certain circumstances leading to erroneous conclusions.

GROOM-BAILEY DECOMPOSITION

The notion of noninductive galvanic distortion of the electric field by a 3-D surficial feature was first introduced by Larsen (1977) for a one-dimensional subsurface (3-D/1-D), and was extended to a two-dimensional subsurface (3-D/2-D) by Richards et al. (1982). This basic model can be written as

$$\mathbf{Z}_{measured} = \mathbf{RCZ}_{2D}\mathbf{R}^T \tag{1}$$

where $\mathbf{R}$ is a rotation tensor, $\mathbf{C}$ is a real 2×2 telluric distortion tensor, and $\mathbf{Z}_{2D}$ is the regional 2-D impedance tensor in strike coordinates. The physical basis for this equation is given by Groom and Bahr (1992) and Chave and Smith (1994).

There have been many approaches suggested to derive the five parameters descriptive of regional conductivity structure (the geoelectric strike, θ, and the two complex impedances of $\mathbf{Z}_{2D}$) from the eight data at each frequency, and Groom and Bailey (1991) compare and contrast some of them. The most appealing to date, used by the majority of MT practitioners, is that of Groom and Bailey (1989), who proposed a tensor decomposition based on a factorization of the telluric distortion tensor $\mathbf{C}$ as a product of modified Pauli spin matrices,

$$\mathbf{C} = g\mathbf{TSA}, \tag{2}$$

where g is a scalar termed "site gain" and $\mathbf{T}$, $\mathbf{S}$, and $\mathbf{A}$ are tensor factors termed *twist, shear*, and *anisotropy*, respectively. This factorization allows a separation of determinable and indeterminable elements of the distortion tensor $\mathbf{C}$, as well as providing some physical insight into the distortion produced by elements of the distortion tensor.

The twist ($\mathbf{T}$) and shear ($\mathbf{S}$) tensors form the determinable portion of the distortion matrix. Note that both of these have amplitude as well as phase effects. The twist tensor rotates the regional electric field clockwise by an angle $\tan^{-1}t$, while the shear tensor develops anisotropy on an axis which bisects the regional principle axis system, rotating a vector on the x-axis clockwise and a vector on the y-axis counter-clockwise by an angle of $\tan^{-1}e$. For a shear e of 1 or -1 (shear angle of 45° or -45°), the electric field becomes totally polarized, and information about the subsurface can only be obtained in the direction of the polarized electric field (which may not be the regional strike direction or perpendicular to it). Accordingly, these values represent physical bounds that can be placed on e during model fitting. Parameters e and t are chosen instead of their arctangent angles for numerical stability in the ensuing model fitting. Contrary to statements made by others, they are not chosen arbitrarily in order to make GB decomposition less intuitive.

The site gain (g) and anisotropy tensor ($\mathbf{A}$) together form the indeterminable parts of the distortion matrix that scale the apparent resistivity curves, and form part of the *static shifts* for each mode (Jones, 1988). In this factorization, the site gain g scales the regional electric field, producing no change in the direction of the electric field, and the anisotropy tensor scales the electric field along the two regional principle axes by different factors, producing a distortion anisotropy which adds to the regional inductive anisotropy. This distortion anisotropy is experimentally indistinguishable from the regional inductive anisotropy without independent information.

Absorbing the site gain g and anisotropy s into the regional impedance, the measured impedance tensor under the GB factorization becomes

$$\begin{aligned}\mathbf{Z}_{measured} &= \mathbf{RTSZ}_{regional}\mathbf{R}^T \\ &= \begin{bmatrix}\cos\theta & -\sin\theta \\ \sin\theta & \cos\theta\end{bmatrix}\begin{bmatrix}1-te & e-t \\ e+t & 1+te\end{bmatrix} \\ &\quad \times \begin{bmatrix}0 & A \\ -B & 0\end{bmatrix}\begin{bmatrix}\cos\theta & \sin\theta \\ -\sin\theta & \cos\theta\end{bmatrix},\end{aligned} \tag{3}$$

where $\mathbf{Z}_{regional}$ is the scaled regional 2-D impedance tensor ($g\mathbf{AZ}_{2D}$). Groom and Bailey (1989) showed that when the measured impedance tensor obeys the decomposition model, the tensor is uniquely described by the seven parameters of the factorization (3), provided that the absolute value of shear e and anisotropy s are less than one (corresponding shear angles between 45° and -45° and distortion anisotropy between 1 and -1). A shear e or anisotropy s (sum of distortion and

regional) of absolute value one produces a singular impedance tensor for which the distortion model becomes underdetermined. Whereas in theory a fully singular tensor is unlikely, in practice experimental noise can cause the impedance tensor to become statistically indistinguishable from singular. This is particularly true in complex, highly resistive terrains with small conductive surface inclusions (Jones, 1988) or in regions of high topographic relief (Jiracek, 1990), where the shear and anisotropy can attain values which produce a virtually singular impedance tensor.

The seven parameters of the GB factorization are the two descriptors of telluric distortion twist t and shear e, the regional strike θ, and the four parameters contained in the two complex scaled regional impedances A and B (Z_{xy} and Z_{yx}). The parameters of the factorization are found by fitting the seven parameters of the decomposition model to the eight data of the measured impedance tensor. This is done by minimizing the χ^2, or least-squared misfit, between the data and model summary decomposition coefficients given by

$$\begin{aligned} \alpha_0 &= Z_{xx} + Z_{yy} \\ \alpha_1 &= Z_{xy} + Z_{yx} \\ \alpha_2 &= Z_{yx} - Z_{xy} \\ \alpha_3 &= Z_{xx} - Z_{yy}. \end{aligned} \tag{4}$$

and

$$\begin{aligned} \alpha_0 &= t\sigma + e\delta \\ \alpha_1 &= (\delta - et\sigma)\cos 2\theta - (t\delta + e\sigma)\sin 2\theta \\ \alpha_2 &= -\sigma + et\delta \\ \alpha_3 &= -(t\delta + e\sigma)\cos 2\theta - (\delta - et\sigma)\sin 2\theta, \end{aligned} \tag{5}$$

respectively, where

$$\sigma = A + B$$

and

$$\delta = A - B$$

are the sum and difference of the regional impedances. Equating equations (4) and (5), one obtains four simultaneous complex nonlinear equations which are solved for the seven parameters of the factorization.

In conventional GB analysis, the decomposition model is fit to the measured data frequency-by-frequency and site-by-site (Groom et al., 1993). However, for the 3-D/2-D distortion model to be valid, frequency independent estimates of the twist, shear, and regional strike must be found over a sufficiently wide band of frequencies. In practice this is done by iteratively constraining the estimates of twist, shear, and strike found at each frequency in an attempt to find a frequency band for which the constrained values result in an acceptable misfit error (Groom et al., 1993; Jones and Dumas, 1993). If the regional conductivity structure is truly 1-D or 2-D, the model will hold in general at low frequencies, reducing the task to finding an upper frequency limit below which the distortion becomes solely galvanic (distorter becomes inductively small) and the distortion parameters become frequency independent.

Regional strike estimation

Regional strike is arguably the most important parameter recovered in decomposition analysis of the impedance tensor. Its resolution is a function of frequency and location relative to both the distorting body and the regional 2-D structure, and its recovery is impeded by galvanic distortion and experimental error. Unfortunately, regional strike is often the poorest resolved parameter in decomposition analysis (Jones and Groom, 1993). The importance of accurate recovery of the regional strike can be seen by examining properties of the measured impedance tensor under GB factorization. In an arbitrary coordinate system, the measured impedance tensor is given by equations (5). The elements of the impedance tensor are distortion and rotation-dependent mixtures of the two regional impedances. In the regional coordinate system, however, equations (5) reduce to

$$\mathbf{Z}_{meas}(\theta_{regional}) = \begin{bmatrix} -(e-t)B & (1-te)A \\ -(1+te)B & (e+t)A \end{bmatrix}, \tag{6}$$

and the two columns of the impedance tensor contain scaled estimates of the regional impedances. The impedance elements in the two columns are linearly dependent, having the same impedance phase as recognized by Bahr (1984a, b), differing solely in magnitude. The magnitudes of the four elements are described by the twist (t) and shear (e) factors of the GB factorization. Equation (6) shows that an error in regional strike will result in impedances which are mixtures of the two regional impedances, whereas errors in twist and shear result solely in errors in the magnitudes of the recovered regional impedances. Recovery of the correct regional strike is therefore essential for accurate recovery of the regional impedances.

The linear dependence of the impedance elements in the regional coordinate system is both the basis of the decomposition procedures proposed by Zhang et al. (1987), Bahr (1988), and Chakridi et al. (1992) and the reason conventional 2-D analysis fails. In conventional analysis, the strike angle is found by minimizing the diagonal elements of the impedance tensor:

$$minimize|Z_{xx} - Z_{yy}|^2 \tag{7}$$

(Swift, 1967; Sims and Bostick, 1969). Using equations (5), the minimum becomes

$$\theta' = \theta_{regional} + \frac{1}{2}\tan^{-1}\left(\frac{t\delta + e\sigma}{\delta - et\sigma}\right). \tag{8}$$

Equation (8) shows that in the presence of distortion, the strike angle θ' recovered in the conventional method will be in error.

In the decomposition procedures proposed by Zhang et al. (1987), Bahr (1988), and Chakridi et al. (1992), the linear dependence of the columns of the impedance tensor is used to estimate regional strike. This method is unstable in the presence of noise or strong distortion since some of the elements of the tensor can be small in magnitude and dominated by error, producing significant errors in the estimate of regional strike (Jones and Groom, 1993). Bahr (1988) recognized this problem, and introduced an ad hoc phase deviation parameter, δ, to balance the misfit, but there is no physical basis for this parameter. GB decomposition performs better than rotation in the presence of noise since it simultaneously solves for all of the parameters of the decomposition model. In addition, fitting

a distortion model provides superior estimates of regional parameters than merely rotating the impedance tensor to strike, since much of the amplitude shifts are caused by removable electric field distortions (twist and shear).

EXTENSION OF GB DECOMPOSITION FOR MULTIPLE SITES AND MULTIPLE FREQUENCIES

To improve the estimate of regional strike, we extend GB analysis to fit statistically an entire dataset simultaneously with an assumed 3-D/2-D model of galvanic distortion. Extension of the analysis improves the estimate of regional strike since it accounts for the position and frequency dependence of strike resolution as regional strike is usually only well-defined over a small subset of the data, and the dependence of model misfit on strike defines a regional strike statistically consistent with the entire dataset or data subset.

In the extended GB analysis, S magnetotelluric sites having N frequencies ($S \times N \times 8$ data, for data at every frequency from every site) is fit to $S \times (N \times 4 + 2) + 1$ unknowns. The unknowns are the $S \times N$ regional complex impedances (A and B), the $S \times 2$ descriptors of telluric distortion (twists t and shears e), and the single regional strike angle (θ). The telluric distortion parameters, shear and twist, are site dependent but frequency independent. Assuming that all the data are independent, the model has $S \times (N \times 4 - 2) - 1$ degrees of freedom. In the case of a single site, the extended model is equivalent to that of the GB method with the strike, twist, and shear constrained to be independent of frequency, although the solutions are arrived at differently.

The model parameters are found in the extended analysis by minimizing a misfit function based on the observed and model summary decomposition coefficients given by equations (4) and (5), respectively. The minimization procedure seeks a simultaneous solution to the $S \times N \times 8$ nonlinear equations (4 real and 4 imaginary equations for each of the $S \times N$ impedance tensors) describing the measured data set. An objective functional normalized by the data variances was chosen in order to reduce any bias produced by frequency and position dependence of experimental error and the frequency dependence of impedance magnitudes. Additionally, the objective function allows one to derive significance levels for the parameter estimates obtained by the minimization procedure.

The objective function adopted is given by

$$\gamma^2(a) = \sum_{k=1}^{SN} \left(\sum_{i=0}^{3} \left[\frac{Re\left(\alpha_i^{obs}\right) - Re\left(\alpha_i^{model}(a)\right)}{\sigma_{\alpha_i}} \right]^2 + \sum_{i=0}^{3} \left[\frac{Im\left(\alpha_i^{obs}\right) - Im\left(\alpha_i^{model}(a)\right)}{\sigma_{\alpha_i}} \right]^2 \right) \quad (9)$$

where σ is the standard deviation of the summary coefficients [equations (4) and (5)]. Minimization of the objective function is performed with a sequential quadratic programming algorithm (NAG routine E04UPF). The algorithm iteratively improves a user-supplied trial solution by minimizing a quadratic approximation of the objective function. Iterations proceed until the gradient of the objective function is zero with respect to all parameters, or when successive iterations produce changes in the estimated parameters less than a user-specified tolerance.

For each iteration, the objective function is approximated by an $S \times (N \times 4 + 2) + 1$ dimensional quadratic function derived from a Taylor series expansion of the objective function,

$$\gamma^2(\mathbf{a}) = \gamma^2(\mathbf{P}) + \sum_i \frac{\partial \gamma^2}{\partial a_i} a_i + \frac{1}{2} \sum_{i,j} \frac{\partial^2 \gamma^2}{\partial a_i \partial a_j} a_i a_j + \cdots \approx c + \mathbf{J} \cdot \mathbf{a} + \frac{1}{2} \mathbf{a} \cdot \mathbf{H} \cdot \mathbf{a}, \quad (10)$$

where $\mathbf{a}$ is the parameter set sought by the minimization routine, $\mathbf{c}$ is the value of the objective function for the trial parameter set $\mathbf{P}$, and $\mathbf{J}$ and $\mathbf{H}$ are the gradient (Jacobian) and Hessian of the objective function evaluated at the trial solution. If the approximation is good, the routine can jump from the trial solution $\mathbf{P}$ to the minimum $\mathbf{a}_{\min}$ by minimizing the gradient of the approximation. The gradient of equation (10) is easily calculated as

$$\nabla \gamma^2 \approx \mathbf{H} \cdot \mathbf{a} + \mathbf{J}. \quad (11)$$

The approximate objective function will be at its minimum when the gradient vanishes. The minimum ($\mathbf{a}_{\min}$) therefore satisfies

$$\mathbf{H} \cdot \mathbf{a}_{\min} + \mathbf{J} = 0. \quad (12)$$

For the trial solution, the gradient is

$$\nabla \gamma^2(\mathbf{P}) = \mathbf{H} \cdot \mathbf{P} + \mathbf{J}. \quad (13)$$

Subtracting equation (17) from equation (18), we obtain an equation for the minimum ($\mathbf{a}_{\min}$):

$$\mathbf{a}_{\min} = \mathbf{P} - \mathbf{H}^{-1} \cdot \nabla \gamma^2(\mathbf{P}). \quad (14)$$

If the approximation is reasonable, and we can calculate the gradient and Hessian of the objective function, the minimization algorithm we use can find the minimum of the objective function in one iteration.

Since equation (10) may be a poor local approximation to the true objective function, the inverse Hessian in equation (14) is replaced by a constant determined from the magnitude of the Hessian. This constant is small enough to allow the algorithm to take a step down the gradient without exhausting the downhill direction. Successive approximations of the objective function iteratively approach the desired minimum ($\mathbf{a}_{\min}$) of the objective function in a damped stepwise fashion.

The exact value of the Hessian has no effect on the final set of parameters $\mathbf{a}_{\min}$ reached by the algorithm. The Hessian's value only affects the iterative route to the minimum. This saves computation time by using an approximation to the Hessian. Writing the summary coefficient equation differences as an $S \times N \times 8$ vector

$$\gamma_i(a) = \frac{\alpha_i^{obs} - \alpha_i^{model}(a)}{\sigma_{\alpha_i}} \quad i = 1, 2, \ldots, S \times N \times 8, \quad (15)$$

the objective function becomes

$$\gamma^2(a) = \sum_{i=1}^{SN8} [\gamma_i(a)]^2. \quad (16)$$

Taking the first derivative of equation (15), the Jacobian of the summary coefficient difference vector becomes a [$S \times$

$N \times 8] \times [S \times (N \times 4 + 2) + 1]$ matrix given by

$$\frac{\partial \gamma_i(a)}{\partial a_j} = \frac{-1}{\sigma_{\alpha_i}} \frac{\partial \alpha_i^{model}(a)}{\partial a_j} \qquad i = 1, 2, \ldots, S \times N \times 8$$
$$j = 1, 2, \ldots, S \times (N \times 4 + 2) + 1. \tag{17}$$

The Jacobian (gradient) of the objective function, a $S \times (N \times 4 + 2) + 1$ element vector containing sums of the partial derivatives of the $S \times N \times 8$ subfunctions (four real and four imaginary equations for each of the modeled tensors), can be found using equations (16) and (17):

$$\frac{\partial \gamma^2(a)}{\partial a_i} = 2 \sum_{j=1}^{S \times N \times 8} \gamma_j(a) \frac{\partial \gamma_j(a)}{\partial a_i}$$
$$i = 1, 2, \ldots, S \times (N \times 4 + 2) + 1. \tag{18}$$

Taking an additional partial derivative we obtain the Hessian of the objective function, an $[S \times (N \times 4 + 2) + 1] \times [S \times (N \times 4 + 2) + 1]$ matrix of second partial derivatives:

$$\frac{\partial^2 \gamma^2}{\partial a_i \partial a_j} = 2 \sum_{k=1}^{SN8} \frac{1}{\sigma_{\alpha_k}^2} \left[\frac{\partial \alpha_k^{model}(a)}{\partial a_i} \frac{\partial \alpha_k^{model}(a)}{\partial a_j} + \left[\alpha_k^{obs} - \alpha_k^{model}(a) \right] \frac{\partial^2 \alpha_k^{model}(a)}{\partial a_i \partial a_j} \right]. \tag{19}$$

Note that the equation for the Hessian (19) contains terms in both first and second derivatives of the summary coefficients. For a successful model, the term containing the second derivative in equation (19) becomes negligibly small. The multiplier $[\alpha^{obs} - \alpha^{model}]$ approaches the random measurement error of the summary coefficient, and the second derivative terms cancel each other on summation. The Hessian can therefore be approximated by the first derivative term in equation (19). Using equation (17), the approximate Hessian becomes

$$\frac{\partial^2 \gamma^2(a)}{\partial a_i \partial a_j} \approx 2 \sum_{k=1}^{SN8} \frac{\partial \gamma_k(a)}{\partial a_i} \frac{\partial \gamma_k(a)}{\partial a_j}$$
$$i, j = 1, 2, \ldots, S(N4 + 2) + 1. \tag{20}$$

Therefore, to preform the minimization one needs only to calculate equations (15) and (17), from which the objective function, gradient, and approximate Hessian can be obtained.

Assuming both the observed and modeled parameters, α_i, have Gaussian distributions, this functional is distributed as χ^2, and we can apply standard tests for goodness of fit between the data and the model.

Error estimation

Derivation of confidence intervals on the estimated regional impedances is complicated by two factors: (1) the transformation between measured and 2-D regional impedances is nonlinear and therefore the parameters do not have a linear dependence on the noise; (2) the distribution of the measured impedance elements is unknown. This lack of knowledge about the distribution of the impedance elements prevents the use of parametric techniques to estimate confidence limits.

Groom and Bailey (1991) derived confidence limits using a bootstrap procedure to determine the scatter of recovered parameters found by fitting decomposition models to realizations of the measured impedance elements. These realization are generated by adding random Gaussian noise, with variance equal to that estimated for the impedances, to the measured impedances. Chave and Smith (1994) use a jackknife technique to determine confidence intervals on the regional impedances by fitting decomposition models to successive jackknife estimates of the measured impedances. This method is superior since it makes no assumptions about error distribution, but requires all the individual estimates of the measured impedances tensor, not just the mean values and their variances.

As the jackknife method cannot be performed without reprocessing from time series, we use the bootstrap method of Groom and Bailey (1991) to derive the desired confidence limits, with one difference that the error bounds are derived from a jackknife procedure rather than a parametric estimator.

Failure of decomposition analysis

There are two situations that can occur in decomposition analysis of the impedance tensor where the method fails to recover the regional impedances accurately. Decomposition fails when the shear angle approaches $\pm 45^\circ$ (e of ± 1) or when the sum of distortion anisotropy (s) and regional anisotropy approaches one. The former is termed class 6 in Bahr's (1991) classification scheme. In both situations, decomposition analysis fails because the measured impedance tensor approaches singularity and the decomposition model becomes underdetermined.

In the case of high shear (high e), the measured impedance tensor approaches

$$Z_{meas}(\theta_{regional}) = \begin{bmatrix} -(1-t)B & (1-t)A \\ -(1+t)B & (1+t)A \end{bmatrix} \tag{21}$$

in the regional coordinate system. The two rows of the impedance tensor become linearly dependent. In fact, the two rows of the impedance tensor are linearly dependent in any coordinate system. The strike therefore is unresolvable, as the impedance tensor assumes the form of a distorted 2-D tensor [equation (9)] in any coordinate system. The shear angle ($\tan^{-1} e$) will be well resolved by the linear dependence of the two rows, although only the sum of the regional strike and twist angles will be resolved. The twist t becomes

$$t(\theta) = t - \tan(\theta - \theta_{regional}) \tag{22}$$

where $(\theta - \theta_{regional})$ is the regional strike error. In order to recover the regional impedances, the strike must be found from adjacent sites or other independent information.

In the high anisotropy case, the measured impedance tensor in the regional coordinate system will approach one of two forms:

$$Z_{meas}(\theta_{regional}) = \begin{bmatrix} -(e-t)B & 0 \\ -(1+te)B & 0 \end{bmatrix} \tag{23}$$

or

$$Z_{meas}(\theta_{regional}) = \begin{bmatrix} 0 & (1-te)A \\ 0 & (e+t)A \end{bmatrix}. \tag{24}$$

The distortion parameters will not be resolved and, while a strike angle is recovered, it cannot be determined if it is that of the regional structure or a local distorter. If the strike determined by decomposition is in agreement with the regional

strike found at other nearby sites (in an inductive sense), it may be reasonable to assume that the recovered impedance is one of the two regional impedances.

EXAMPLES OF APPLICATION

Synthetic example 1

To illustrate the performance of the proposed decomposition procedure in the presence of experimental noise, noisy realizations of the same distorted synthetic impedance tensor used by Jones and Groom (1993) were generated. The theoretical response is taken from a 2-D model of the North America Central Plans (NACP) conductivity anomaly (Jones and Craven, 1990), and is an impedance tensor for maximum induction in the body. To derive a distorted response the distortion matrix used, Chakridi et al. (1992) was again adopted. The noise-free distorted impedance tensor is given by

$$\mathbf{Z} = \mathbf{C}\mathbf{Z}_{2-D} = \begin{bmatrix} 1.26 & 0.44 \\ 0.53 & 0.86 \end{bmatrix} \times \begin{bmatrix} 0 & (4.72, 4.05) \\ (-8.25, -3.10) & 0 \end{bmatrix} \times 10^{-4}(\Omega) = \begin{bmatrix} (-3.63, -1.36) & (5.95, 5.10) \\ (-7.10, -2.67) & (2.51, 2.15) \end{bmatrix} \times 10^{-4}(\Omega). \quad (25)$$

Decomposition of the distortion tensor above in terms of GB parameters yields a site gain (g) of 1.06, an anisotropy (s) of 0.172, a twist angle of -2.1° ($t = -0.037$), and a shear angle of 24.95° ($e = 0.47$). The inductive strike of the regional structure, is 0°.

Gaussian noise, with standard deviation of 4.5% of the magnitude of the largest impedance element, was added to the tensor (25) to produce 31 noise-contaminated realizations. These 31 realizations form an ideal data set to test the performance of the decomposition procedure in the presence of noise, as all realizations are equally sensitive to the inductive strike and obey the telluric distortion model differing solely by experimental noise.

Figure 1 shows histograms of the strike, twist, and shear found from an unconstrained GB analysis of the 31 realizations. As reported in Jones and Groom (1993), the distributions of the GB parameters clearly shows that shear and twist are more stable under distortion decomposition than strike angle determination. The strike directions determined appear to be approximately normally distributed, although they poorly define the regional strike. This example clearly corroborates the difficulty in obtaining an accurate estimate of the regional strike in the presence of distortion and experimental noise reported by Groom et al. (1993) and Jones and Groom (1993). These synthetic realizations are for maximum induction in the anomaly and, as such represent, a best case scenario for strike determination.

The results of the extended decomposition analysis yield a twist angle of -2.2°, a shear angle of 25.6°, and strike direction of 0.16°, very close to the correct values of -2.1°, 24.95°, and 0°, respectively. The results appear to be accurate and free of noise bias, in contrast to the outcome of iteratively constraining the frequency-dependent decomposition parameters advocated by Groom et al. (1993). Such a procedure resulted in an estimate of strike of $-7^\circ \pm 4^\circ$ (Jones and Groom, 1993). Although the data set is somewhat unrealistic, the performance of the extended decomposition analysis indicates that if the 3-D/2-D model is applicable to real data, the extended GB analysis should yield a stable estimate of strike direction in the presence of experimental noise.

Synthetic example 2

We now consider the question of decomposition analysis of a more realistic theoretical response, where sensitivity to the 2-D inductive strike is a function of frequency. Groom and Bailey (1991) produced an accurate 3-D/2-D data set by superposing 3-D analytic and 2-D numerical responses. The 3-D analytical response is that of a small conducting hemisphere, and the 2-D host is a faultlike structure. Decomposition of the 3-D/2-D theoretical response has been previously discussed by Groom and Bailey (1991) and Groom et al. (1993). For the frequencies considered, the hemisphere has negligible inductive response (West and Edwards, 1985), but has a significant effect on both the electric and magnetic fields of the regional 2-D structure. For frequencies lower than 10 Hz (periods longer than 0.1 s), the distortion effects produced by the anomalous magnetic fields of the hemisphere become negligible, and the hemisphere acts as a galvanic scatterer. Decomposition analysis should recover the regional 2-D impedances to within amplitude scaling shifts at periods greater than 0.1 s.

The strike of the regional 2-D structure is 30°. Groom et al. (1993) showed strike is poorly defined at both short and long periods. For short periods, the data are not sensitive to the 2-D boundaries of the regional structure and are essentially 1-D, whereas at long periods the 2-D structure becomes inductively thin, having only a galvanic response which combines with the galvanic response of the hemispherical distorter. The phases of the two regional impedances become virtually identical and the

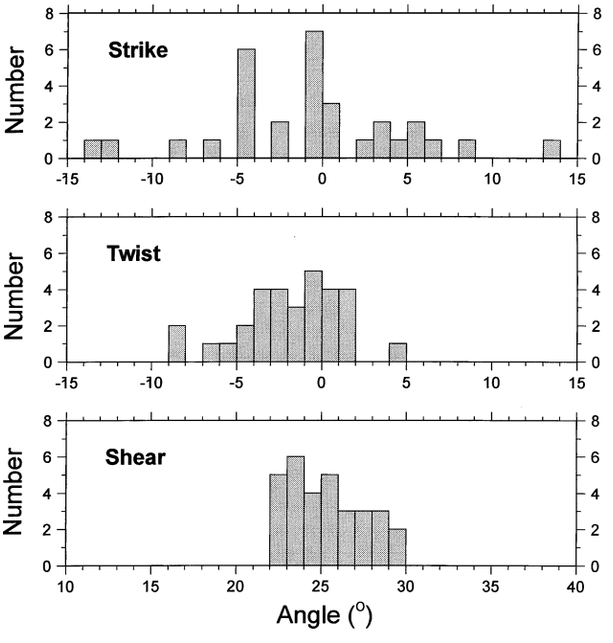

FIG. 1. Distortion parameters determined from single frequency analysis of synthetic dataset example 1.

regional response becomes an anisotropic 1-D response (2-D galvanic distortion of the response of the deep regional 1-D structure, 2-D/1-D). Noise-free decomposition analysis yields a twist angle of -12° and shear angle of 30° (Groom et al., 1993). The 3-D scattering effects of the hemisphere in this data set are first-order effects while the inductive response of the 2-D structure has a much smaller effect, making this a good dataset for testing the extended decomposition routine.

To simulate experimental observations, 2% Gaussian noise and scatter was added to the theoretical responses. Figure 2 shows histograms of the regional strike, twist, and shear angles resulting from conventional GB analysis. Twist and shear angles are reasonably well resolved, although they both exhibit bias as the results are not distributed about the correct values. Although the estimates of regional strike, twist, and shear are scattered, Groom et al. (1993) have shown that reasonable parameter estimates can be determined by iteratively constraining their values (strike 30°, shear 29°, and twist -11°).

The results of the extended decomposition analysis are shown superimposed on the results of the unconstrained GB analysis in Figure 3. The extended analysis yields a strike direction of 30.7°, twist angle of -13.0°, and shear of 30.6°. The extended model has 69 degrees of freedom, with a 95% confidence level having a χ^2 value of 90.0. The χ^2 misfit of the model is 49.5, well below the 95% confidence level.

The recovered and undistorted regional responses are shown in Figure 4. The extended analysis recovers each of the regional responses to within a multiplicative amplitude shift factor. The magnitude and phase of the Z_{yx} (transverse magnetic, or TM, mode) impedance are contaminated by noise at long periods where the Z_{yx} impedance is small in magnitude. This noise contamination is enhanced by the distortion anisotropy, which reduces the magnitude of the Z_{yx} impedance. However, the long period Z_{yx} impedances would have the highest scatter even in the absence of distortion due to their small magnitude.

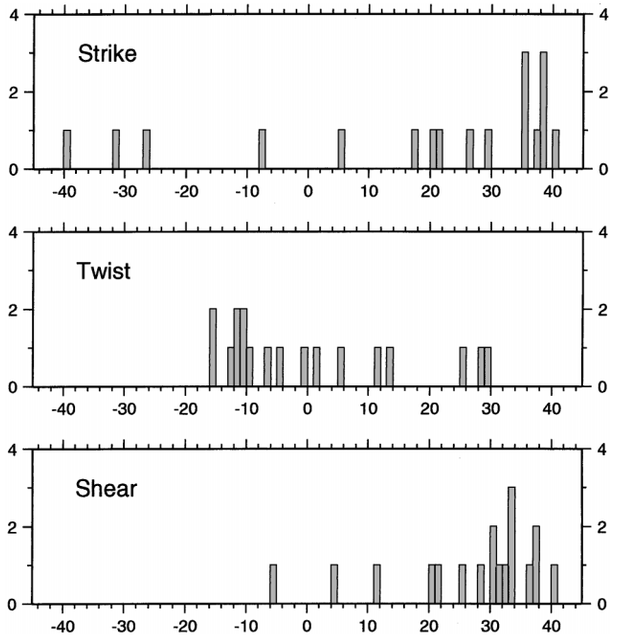

FIG. 2. Distortion parameters determined from single frequency analysis of synthetic dataset example 2.

Synthetic example 3

As a final synthetic example, we consider simultaneous decomposition analysis of an entire dataset. Data at ten MT sites above a given conductive structure (Figure 5) were calculated using Wannamaker's PW2D finite element algorithm (Wannamaker et al., 1985). The ten synthetic regional 2-D impedances were distorted by multiplication with different synthetic distortion matrices (galvanic telluric distortion only).

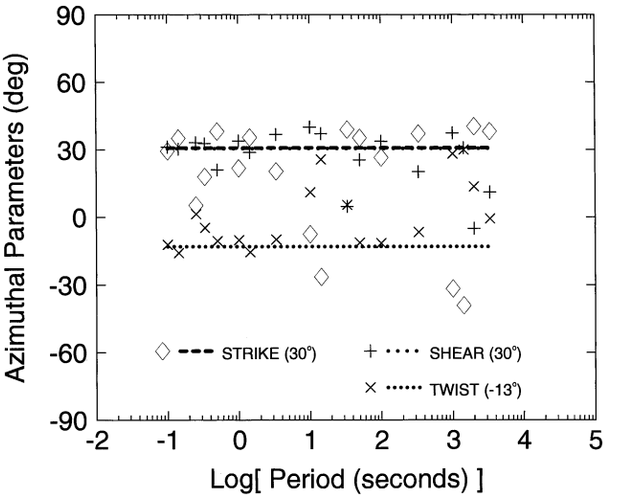

FIG. 3. Comparison of single-frequency decomposition (symbols) with multifrequency decomposition (lines) for synthetic dataset example 3.

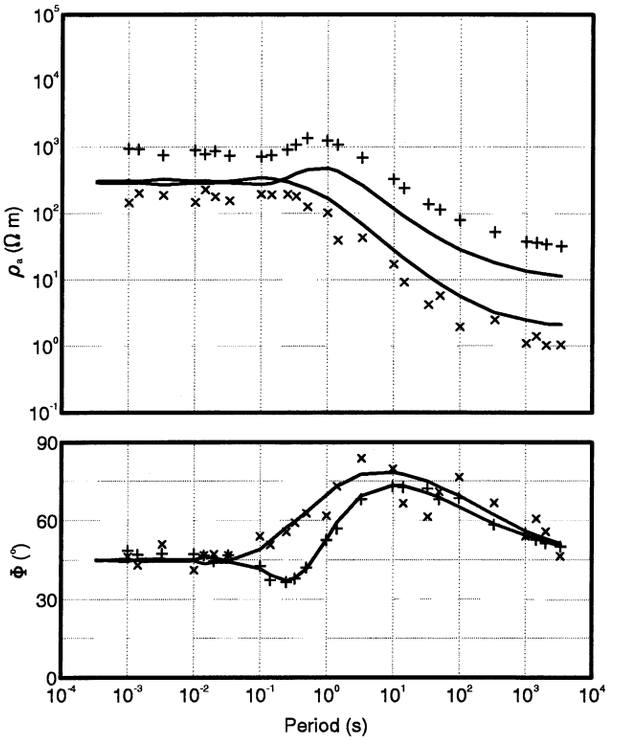

FIG. 4. The recovered regional responses (symbols) compared to the true theoretical responses (solid lines) for synthetic dataset example 2.

Twist and shear values of the synthetic distortion matrices applied to the data are listed in Table 1. Gaussian noise and scatter having a magnitude of 2% of the largest impedance element was added to the distorted responses to simulate experimental noise.

Plots of the decomposition parameters found by unconstrained GB analysis of the synthetic data set are shown in Figure 6. Examination of these plots indicates that, for virtually all of the sites, twist and/or shear are well-resolved parameters. However, the regional strike is poorly resolved for many of the sites. This example clearly demonstrates the effects that galvanic distortion, noise, and insufficient sensitivity to the regional 2-D body can have on the resolution of strike.

The results of simultaneous decomposition of the ten sites are given in Table 1. The extended decomposition derived a regional strike of 30.3°, very close to the correct value of 30.0°. Additionally, accurate estimates of the twist and shear angles were obtained, enabling accurate recovery of the regional responses (not shown). The extended decomposition model has 1219 degrees of freedom, with a 95% confidence level of 1303.4. The χ^2 misfit of the model was 512, well below the 95% confidence level.

Real data example—Papua New Guinea

This example is from a ten-station MT dataset taken in the Kube Kabe ranges of the highlands of Papua New Guinea (PNG) (site locations are shown in Figure 7). A description of the dataset can be found in Jones and Schultz (1997). At each station, MT fields were acquired in the band 384 Hz–0.000549 HZ (1820 s). However, the focus of the survey was the uppermost crust, and hence there was insufficient recording time for precise estimates at long periods. Conventional (Swift, 1967) strike direction estimation, which is based on the magnitudes of the impedance elements rather than their phase relationships, yields a large scatter with frequency and site (see Figure 2 of Agarwal and Weaver, 1997). Using a step-wise approach of rotating the data by 1° increments, fitting frequency-independent shear and twist to each site, and summing the site misfits, Toh and Uyeshima (1997) derived a minimum-misfit global strike direction of N60°W (N30°E) for the whole frequency range of 384–0.01 Hz. Pous et al. (1997)

Table 1. Results of decomposition of synthetic 2-D data set. Joint decomposition found a regional strike of 30.3°, close to the real value of 30.0°.

	True Value		Decomposition Result	
Site	Shear (°)	Twist (°)	Shear (°)	Twist (°)
SYN001	20.0	−20.0	20.1	−20.1
SYN002	−10.0	40.0	−10.1	40.2
SYN003	25.0	−15.0	−25.2	−15.1
SYN004	40.0	20.0	39.9	19.7
SYN005	−25.0	−40.0	−25.0	−40.0
SYN006	−20.0	30.0	−20.2	30.1
SYN007	−35.0	−50.0	−34.9	−50.1
SYN008	25.0	−10.0	25.1	−10.1
SYN009	35.0	−5.0	35.1	−5.3
SYN010	15.0	45.0	14.8	45.1

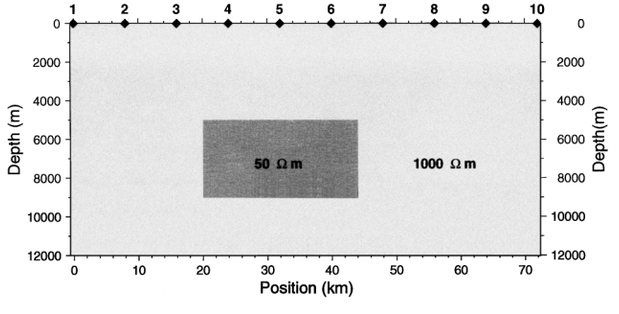

FIG. 5. Conductivity model for synthetic example 3. A 50 ohm-m 2-D body, 5 km deep with a 4 km depth extent and a width of 25 km, is embedded in a 1000 ohm-m half-space. Observations are made at ten sites equispaced at 8 km intervals across the surface.

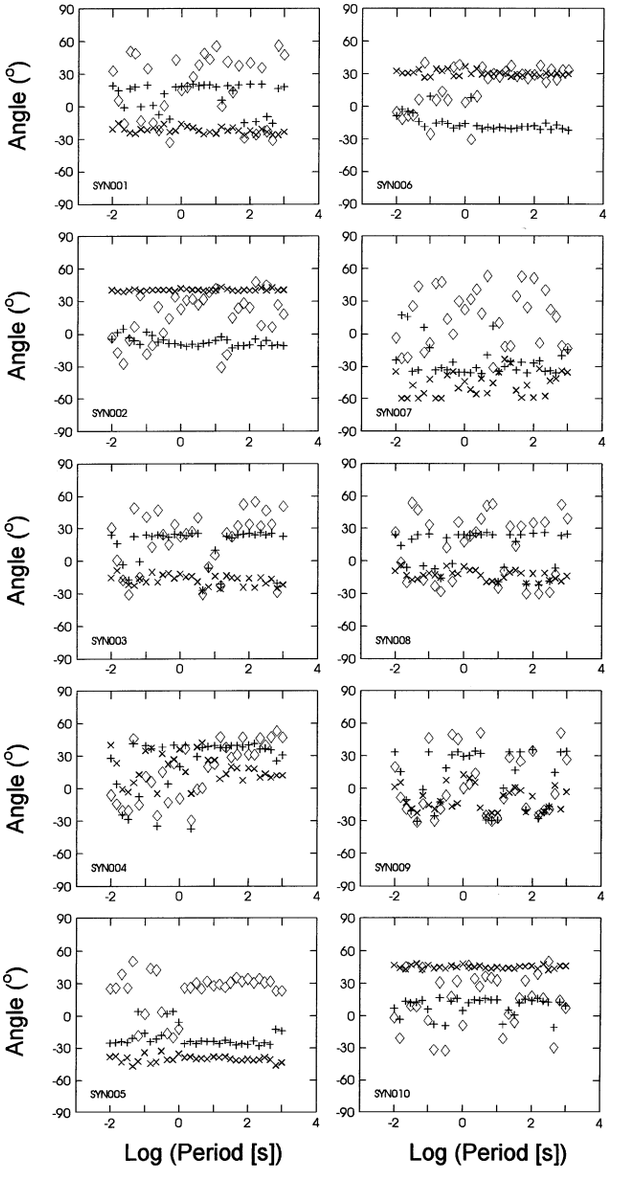

FIG. 6. Frequency and site-independent ecomposition parameters shear (+), twist (×) and strike (diamonds) for the ten sites in Figure 5.

used a similar technique and came up with exactly the same strike angle of N60°W (N30°E).

Single-site, single-frequency decompositions for these data are shown in Figures 8 a–h for sites 101–108, and in Figures 9a–b for neighboring sites 121 and 122 (shown as sites 1–8 and 21–22, respectively, in Figure 7). In all figures, there is an apparently poor rms misfit in a band centered around 0.5 s. Chave and Jones (1997) showed this to be due to overly-optimistic error bounds computed from parametric estimators used in the analysis codes of the contractor which are inaccurate for a large number of estimates. In contrast, the parametric error estimates at longer periods (>20 s) are usually too large (by factors of three to five) compared with the nonparametric jackknife estimates (Chave and Jones, 1997). For the data from site 121, the rms misfits are large at all periods shorter than about 5 s, typically around 20, indicating that the 3-D/2-D galvanic-only distortion model is inadequate. Although sites 121 and 122 are in close proximity (only some 400 m apart), there are different 3-D effects at both locations due to different near-surface structures. The composite of all unconstrained strikes exhibits wide scatter at all periods, with a weak preference of around 25°–30° in the period band 10–100 s (Figure 10). The average rms errors exhibit large values in the band 0.333–1 s, which can be attributed to the parametric error estimator. Generally, a galvanic distortion model is acceptable for these data, excluding sites 121 and 122, and there is relatively weak distortion with shears and twists all typically less than 10°.

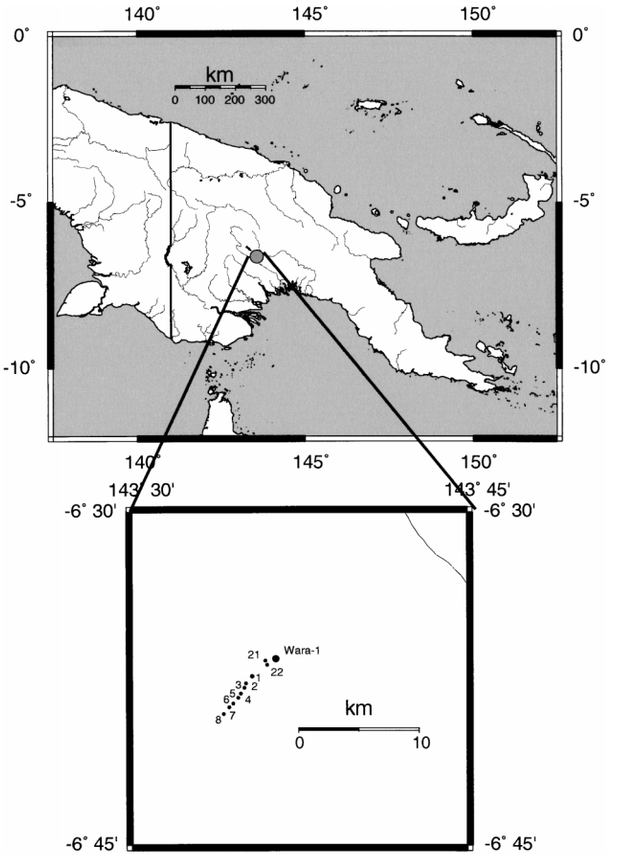

FIG. 7. Site locations for the Papua New Guinea Kube Kabe survey.

The focus of the survey was to determine the subsurface geometry of the Darai limestone that crops out as a series of multiply thrust-faulted anticlinal structures, and provides traps for the oil within the underlying Toro sandstone (Jones and Schultz, 1997; see also Hoversten, 1996). Accordingly, restricting the analysis to the band 384 Hz–10 s, and excluding sites 121 and 122 due to their 3-D behavior, we can derive the strike direction that is most consistent with each frequency from all sites using the multisite mode (Figure 11). The strikes that best fit all sites simultaneously show a preference for around +30°, but there is an apparent visible trend of decreasing strike with increasing period, which can be investigated by undertaking multifrequency and multisite decomposition.

Figure 12 shows the strike and average error for distortion decomposition with a bandwidth of half a decade, and Figure 13 for a full decade. Both of these plots exhibit a moderate frequency dependency (i.e., depth dependency) of strike azimuth, with 28° for the very near surface, rising to 34° for depths of 500–1500 m equivalent to a period band around 0.1 s (10 Hz), then decreasing to a deeper strike of 21° for depths beyond 2500 m (periods >2 s). The best-fitting strike direction determined for all frequencies in the range 384 Hz–0.1 Hz (10 s), and for all sites, is 26.3°(±0.2°), which represents a statistical compromise between the shallower and deeper strike directions. Ogawa (1997), using our code, found the same strike dependency, with strike angles of 33°, 24°, and 18° in period bands of 1–10 s, 10–100 s, and 100–1000 s, respectively.

The focus of the survey was to define structures at depths in the range 1500–2500 m, and so a strike of 34° is appropriate for the problem being studied. The average strike is 8° different from this, and hence interpretation in the averaged direction will not result in as accurate a model for the structures at the depths of interest (1500–2500 m) as interpretation with a strike of 34°. Marquis et al. (1995) and White et al. (1999) also found frequency dependency of strike direction, implying depth dependency of structural strike.

ROTATION OF MT IMPEDANCE TENSOR

It is important to recognize that the regional impedances and confidence limits found solely by rotating the measured impedances are not equivalent to those found through decomposition analysis, even if the regional strike is accurately known (Jones and Groom, 1993). When the measured impedance tensor is rotated to the regional coordinate system, each column of the tensor contains two estimates of one of the regional impedances [see equation (5)]. In rotation methods, the rotated antidiagonal impedances are used as estimates of the regional impedances. In the absence of noise, the antidiagonal elements are algebraically-scaled estimates of the galvanically-distorted true regional impedances, but they do not represent the best estimates of the regional impedances in the presence of noise. Depending on the values of the distortion parameters, twist and shear, one of the diagonal impedance elements (Z_{xx} or Z_{yy}) may contain a better estimate of a regional impedance. This can be seen by examining Figure 14, which shows plots of the ratios of the diagonal and antidiagonal impedances magnitudes (Z_{yy}/Z_{xy} and Z_{xx}/Z_{yx}) as a function of twist and shear. When the sum of the absolute shear and twist angles exceeds 45° (indicated in Figure 14 by the shaded regions), one of the diagonal impedances exceeds the antidiagonal impedance in magnitude.

The larger magnitude estimate of the regional impedance will typically have a greater signal-to-noise ratio and accordingly yields a superior estimate of the regional impedance. Rotation does not account for the scaling produced by galvanic distortion and will result in inferior estimates of the regional impedances. Decomposition analysis, on the other hand, performs essentially a weighted average of the two estimates of each regional impedance, providing a superior estimate in the presence of galvanic distortion and equivalent estimate in the absence of distortion.

Figure 15 shows a comparison of the regional impedances (apparent resistivity and phase) recovered by rotation and

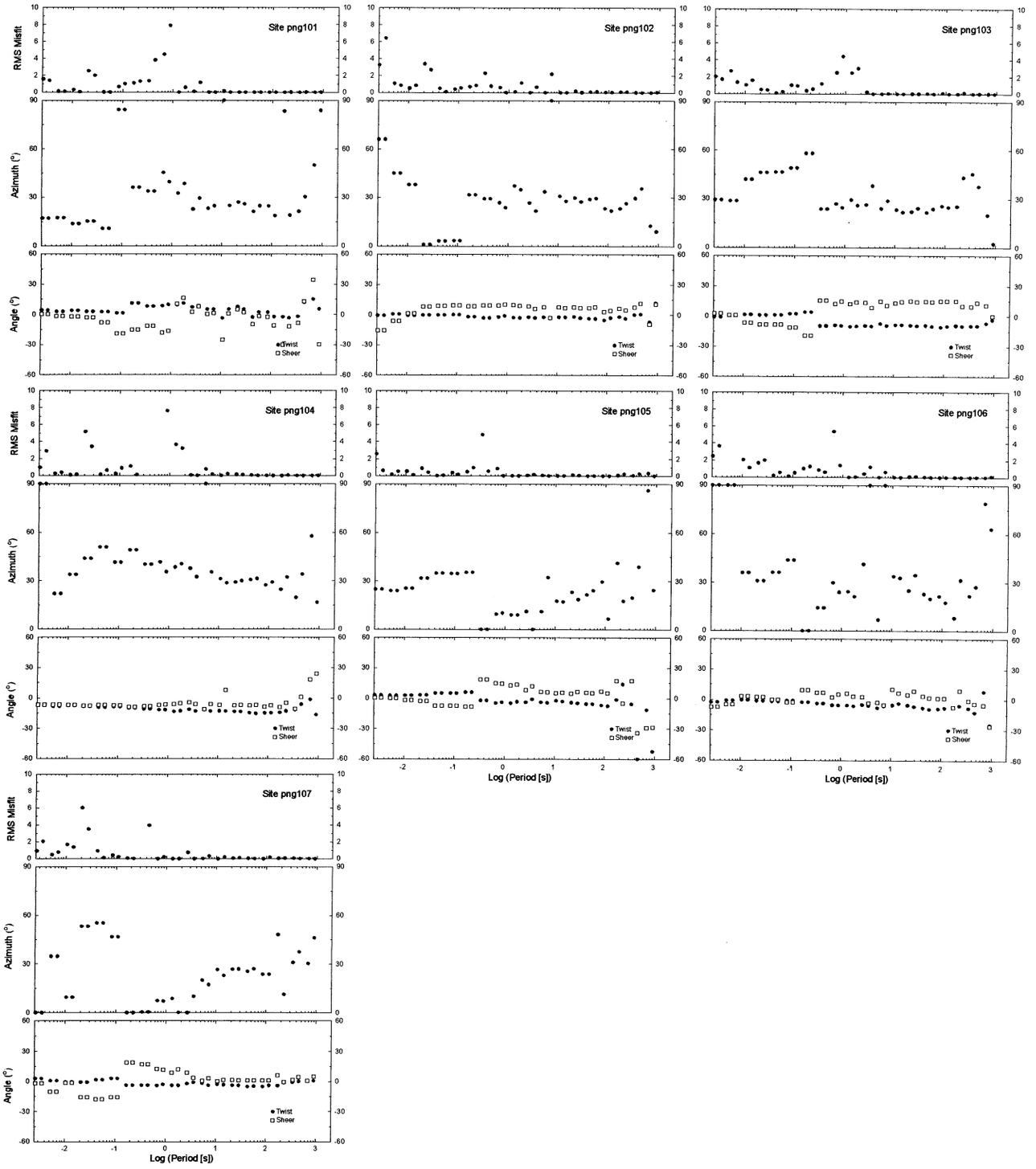

FIG. 8. Frequency-independent GB decompositions for PNG sites 101–108.

decomposition analysis. The data used in this comparison is that of site SYN004 from the synthetic 2-D data set, having a regional strike of 30.0°. The synthetic data from this MT site was distorted by applying a twist of −35°, shear of 25°, and distortion anisotropy of 0.3. Three percent Gaussian noise and scatter were added to the distorted data to simulate experimental error. The true regional strike and distortion parameters were used in the recovery of the regional impedances; however, the extended decomposition analysis was able to recover the values accurately (shear −35.0°, twist 25.1°, and strike 29.9°). The example clearly shows that decomposition recovers superior estimates of the regional impedances.

EXTENSION TO INCLUDE MAGNETIC EFFECTS

At periods longer than those important for inductive effects, the effects of the charges impressed on the surface of the body as a consequence of Ohm's Law and the continuity of current density remain for all periods to d.c. These galvanic charges have both magnetic and electric effects, and in our discussion above only the latter was considered. However, the magnetic effects of the charges can be significant, and Groom and Bailey (1991) describe how to calculate them for a conducting hemisphere. They were first considered by Berdichevsky and Dmitriev (1976), who showed that the magnetic effects are a function of the intrinsic regional impedance, so their importance decreases with increasing period as impedance naturally decreases. Singer (1992) discusses the limits of validly adopting a distortion model of the form of equation (1), which ignores the magnetic effects. Recently, Ritter and Banks (1998) discuss the effects of magnetic effects on geomagnetic depth sounding (GDS) estimates, and propose a method for their removal.

Zhang et al. (1987), Groom (1988), Groom and Bailey (1991), Chave and Smith (1994), and Smith (1997) describe the effects of this electrostatic anomalous magnetic field in terms of a real 2×2 distortion channeling tensor, $\mathbf{D}$ [$\mathbf{Q_h}$ in Zhang et al. (1987), $\mathbf{C}$ in Smith (1997)], that modifies the measured

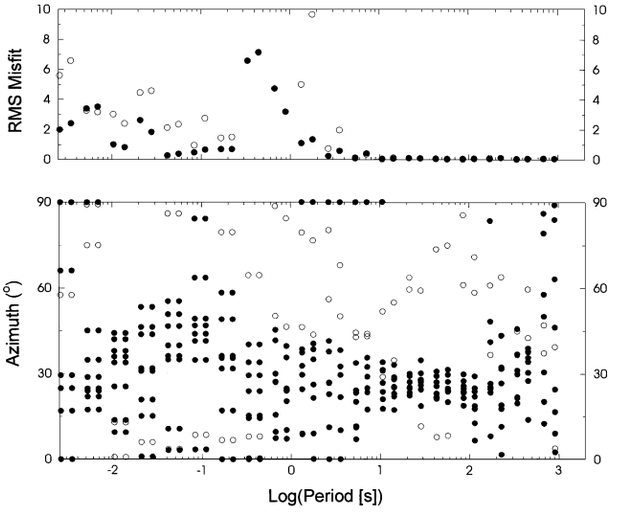

FIG. 10. Sum of strike directions and composite misfit for all PNG sites. Solid circles are for sites 101–108, and open circles are for sites 121–122.

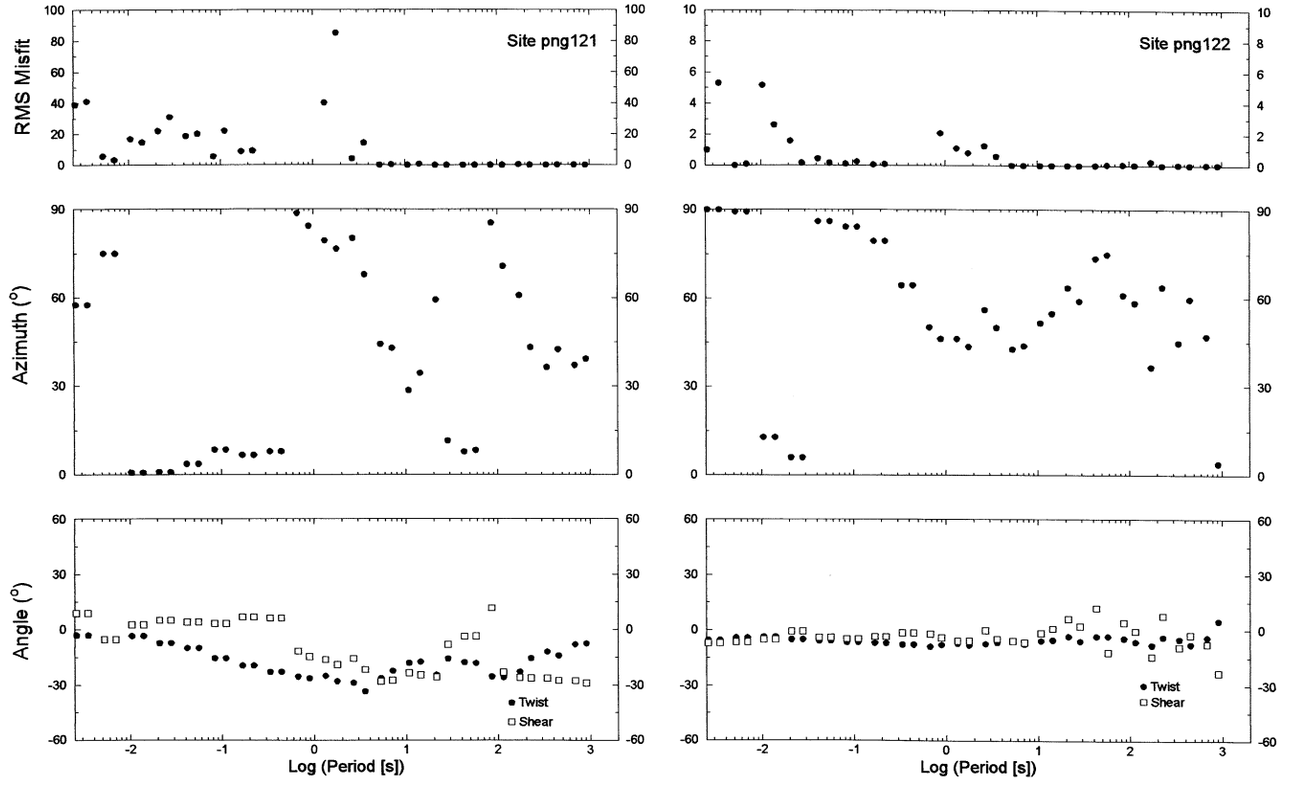

FIG. 9. Frequency-independent GB decompositions for PNG sites 121–122.

MT impedance tensor from equation (1) to

$$\mathbf{Z}_{measured} = \mathbf{RCZ}_{2D}(\mathbf{I} + \mathbf{DZ}_{2D})^{-1}\mathbf{R}^T. \qquad (26)$$

Chave and Smith (1995) derive this equation from first principles using the extended Born approximation of Habashy et al. (1993) and demonstrate that it is impossible to determine uniquely the antidiagonal elements of **D**, and that their indeterminacy is even more extensive than for the static shift factors common to the electric-field only distortion case. Zhang et al. (1993) also recognized this indeterminacy and constrain the solution by assuming orthogonality between the effective magnetic distortion parameters (Zhang et al. 1987).

Note that equation (26) contains 13 variables: the four real elements of **C**, the four real elements of **D**, the real and imaginary parts of the two elements of $\mathbf{Z}_{2D}$, and the strike direction θ. However, due to the indeterminacies, only nine are resolvable; two of the unknowns are the galvanic scaling factors, and the other two are the off-diagonal elements of **D**. As there are only eight data at a particular frequency (real and imaginary parts of each element of $\mathbf{Z}_{meas}$), multifrequency analysis must be undertaken.

In contrast to the effects on the electric field, the effects on magnetic fields occur for a limited frequency range. For a typical embedded inhomogeneity, the magnetic effects occur for less than a decade. Examples can be found in Jones and Groom (1993), Chave and Smith (1994), Chave and Jones (1997), and Smith (1997). This makes determination of the magnetic distortion parameters fraught with instability. The approach that we have taken is a two-step one. In the first step, an electric-field distortion model (1) is fit to the data. Then, the best solution found is used as a starting solution for the full electric and magnetic distortion model (25).

As an example of application of the analysis for magnetic and electric effects, we consider the synthetic data from the embedded hemisphere in a regional 2-D earth considered by Groom and Bailey (1991) and Groom et al. (1993) with an unrealistically small noise component (0.1%) to illustrate the points we wish to stress. The data were analyzed for galvanic distortion using the method previously discussed (synthetic example 2) at periods where the magnetic effect is not important, i.e., longer than 0.1 s (10 Hz). Fitting a frequency-dependent galvanic-distortion model to the data, we find a frequency-dependent strike rotation from $+60^\circ$ at 1000 Hz to $+30^\circ$ by 10 Hz, and a change in the telluric distortion parameters from no distortion rising to values of 30° and -12° for shear and twist, respectively (Figure 16). This conclusion appears to be "confirmed" by a multifrequency analysis over bands a decade in width (Figure 17). Fitting a frequency-independent galvanic-distortion model on the data, the galvanic distortion parameters found are close to the correct values ($29.3^\circ \pm 0.2^\circ$, $30.5^\circ \pm 0.05^\circ$, and $-12.1^\circ \pm 0.05^\circ$, compared to 30°, 30°, and -12°, for strike, shear, and twist, respectively), but the model is clearly inadequate (rms misfit error >1) at frequencies higher than 100 Hz (Figure 18). Accordingly, on the basis of only the

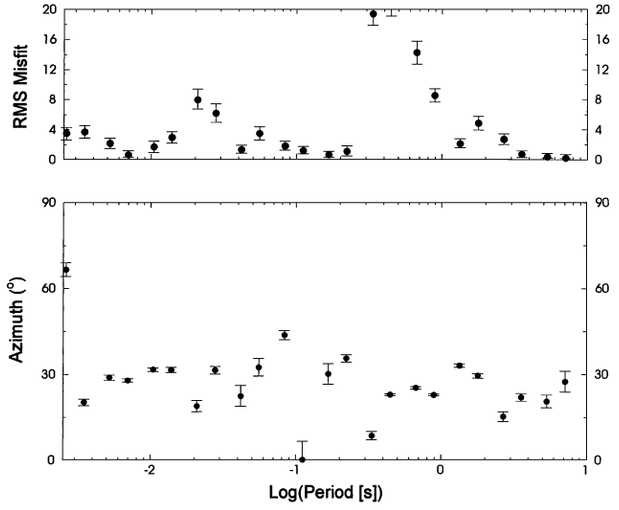

FIG. 11. Misfit error and strike azimuth from multisite decomposition for PNG sites 101–108.

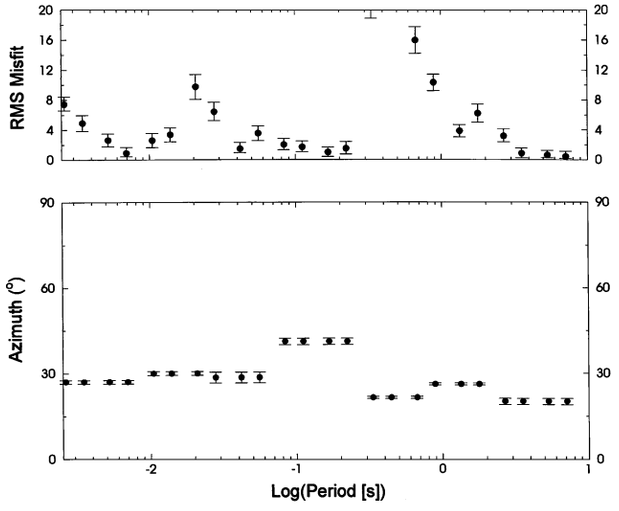

FIG. 12. Misfit error and strike azimuth from multisite decomposition for PNG sites 101–108 constrained over frequency bands of half a decade.

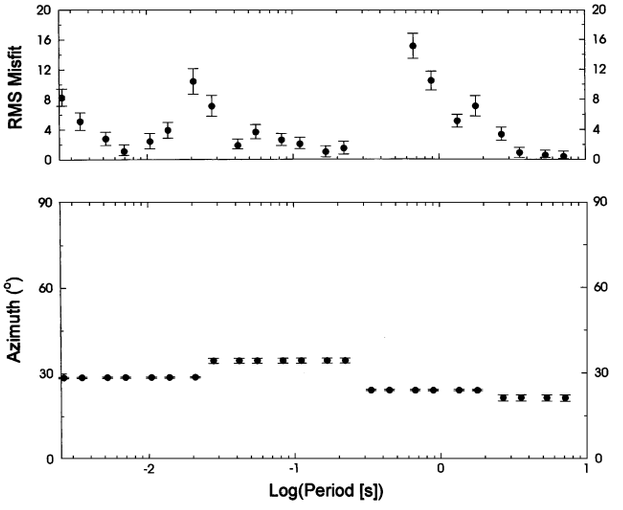

FIG. 13. Misfit error and strike azimuth from multisite decomposition for PNG sites 101–108 constrained over frequency bands of a decade.

observed frequency dependency in strike, shear, and twist, the interpreter would erroneously conclude that the subsurface displays depth-dependent strike, with $+60^\circ$ appropriate for the near surface and $+30^\circ$ for the underlying structures.

A model of magnetic + electric distortion fit to these data in the band 1000 Hz–0.1 Hz (10 s) yields galvanic distortion parameters of $29.98^\circ \pm 0.06^\circ$, $29.86^\circ \pm 0.04^\circ$, and $-12.03^\circ \pm 0.02^\circ$ for strike, shear, and twist, respectively, and magnetic distortion parameters of $D_1 = -0.02055$ and $D_4 = -0.04374$. The data fit is acceptable over the whole range. Even in the problematic range of 1000–100 Hz, the magnetic + electric distortion parameters derived are 29.2°, 30.2°, -11.8°, -0.021, and -0.043 for strike, shear, twist, D_1, and D_2, compared to the derived electric-field only parameters of 49.1°, 10.7°, -7.7°, 0.0, and 0.0.

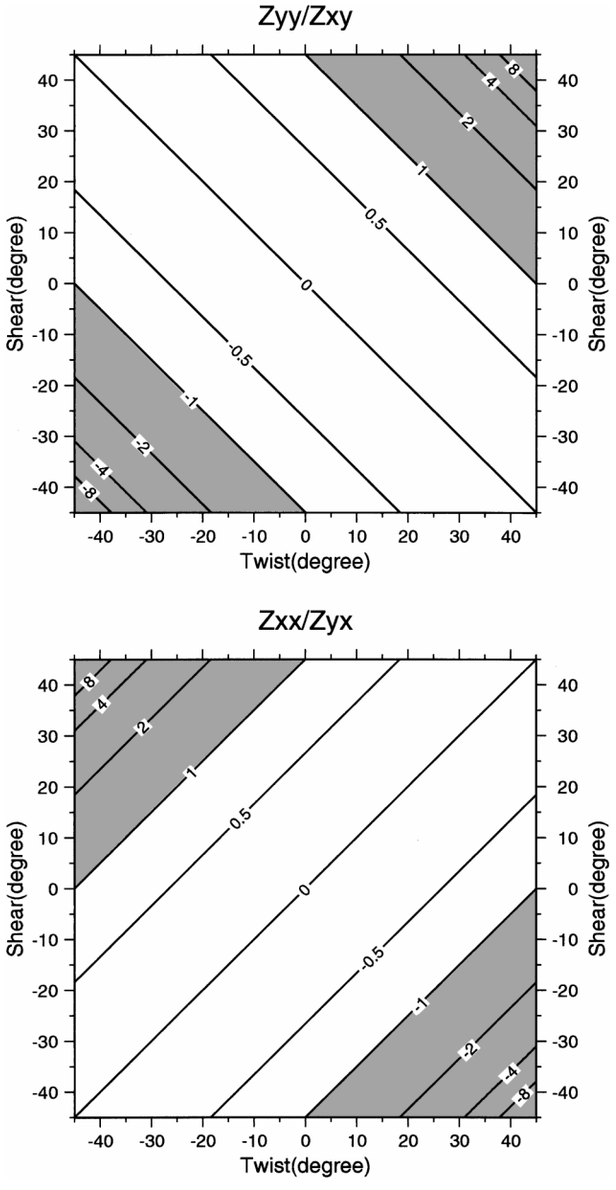

FIG. 14. Ratios of the columns of the impedance magnitudes as a function of twist and shear.

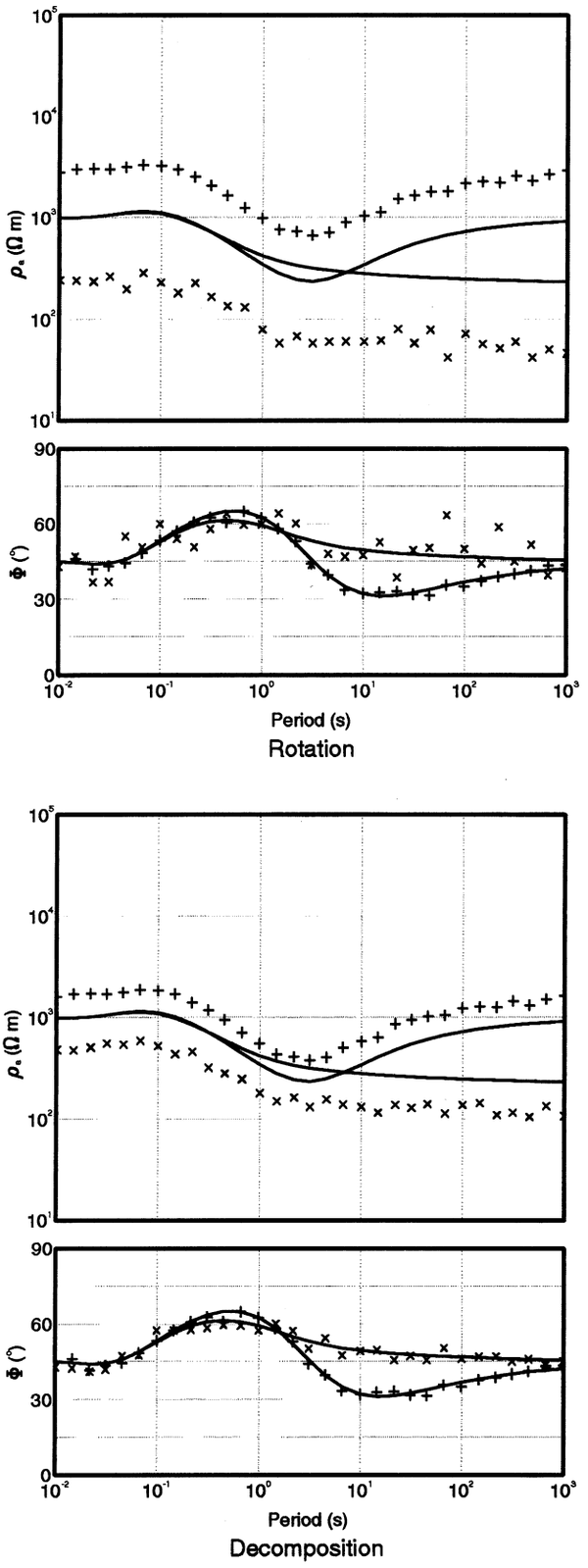

FIG. 15. Comparison of rotation (top) compared to decomposition (bottom) analyses to recover the regional impedances (solid lines) for synthetic example 3 site SYN004.

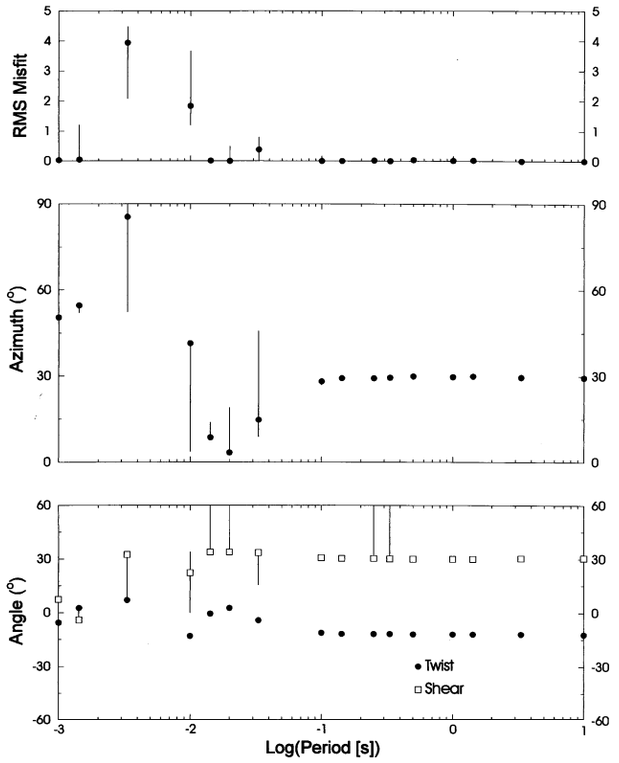

FIG. 16. Electric-only frequency-dependent distortion decomposition for synthetic example 2 with low noise added (0.1%).

CONCLUSIONS

We have extended the GB decomposition method to find the most consistent 2-D parameters from a set of sites over a given frequency band. Our approach includes using an analytical approximate Hessian as a starting solution to increase speed and stability. Both synthetic and real examples demonstrated the superiority of objective multisite, multifrequency analysis over a more subjective approach based on individual site and frequency distortion models.

Including the magnetic effects is possible but must be undertaken with care as the magnetic distortion parameters can be determined over a far smaller frequency range than the electric distortion parameters.

ACKNOWLEDGMENTS

GWMcN acknowledges the Natural Sciences and Engineering Research Council of Canada for financial support, and the Geological Survey of Canada for research facilities during his M.Sc. work. Discussions with David Boerner, Jim Craven, and Ross Groom were very helpful. The PNG data were supplied by Bill Robinson of Chevron (Australia) through an approach made on behalf of the EM induction community by Charlie Swift (Chevron, U.S.A.).

Geological Survey of Canada Contribution No. 1999298. Lithoprobe publication no. 1166.

The software for undertaking multifrequency, multisite MT tensor decomposition described in the paper is available from either author on request.

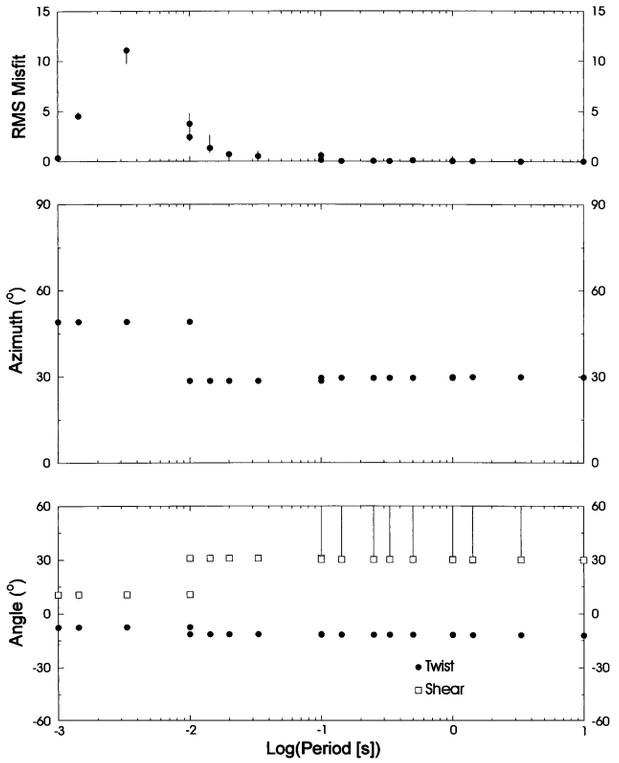

FIG. 17. Electric only multifrequency (one decade width) distortion decomposition for synthetic example 2 with low noise added (0.1%).

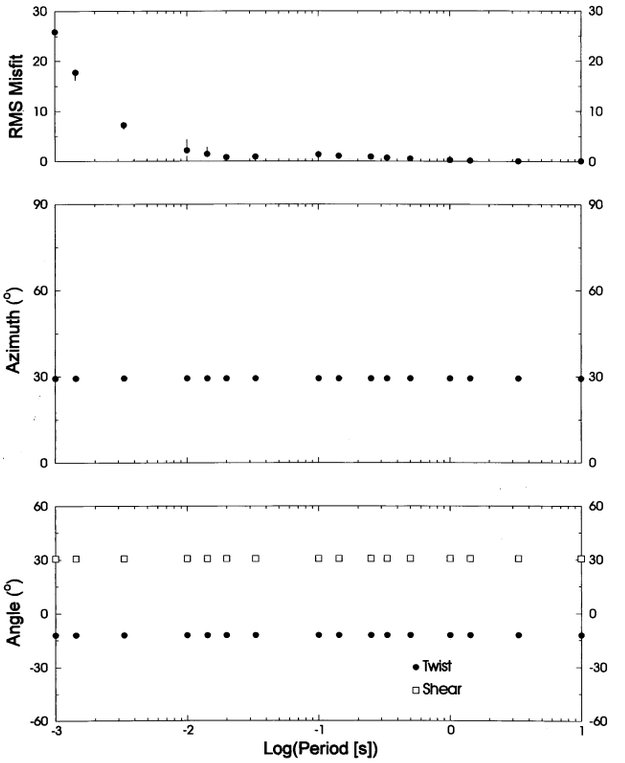

FIG. 18. Electric-only multifrequency (whole bandwidth) distortion decomposition for synthetic example 2 with low noise added (0.1%).

The authors thank reviewers Rob Evans, Karsten Bahr, and an unknown third person, and Associate Editor Xiaobo Li, for their comments on the submitted version of this paper.

REFERENCES

Adam, A., 1998, Tensor decomposition with static shift correction of the deep magnetotelluric (MT) soundings to improve the asthenospheric depth values in the Great Hungarian Plain: Acta Geodaetica et Geophysica Hungarica, **33**, 187–213.

Agarwal, A. K., and Weaver, J. T., 1997, Two-dimensional inversion of Papua New Guinea data using Least-Blocked models: J. Geomagn. Geoelectr., **49**, 827–842.

Bahr, K., 1984a, Ein Beitrag zur Entzerrung des Impedanztensors, *in* Protokol über das 10 Kolloquium "Elektromagnetische Tiefenforschung," 153–164.

——— 1984b, Elimination of local 3D distortion of the magnetotelluric tensor impedance allowing for two different phases: Presented at Seventh Wkshp. Electromagnetic Induction in the Earth and Moon.

——— 1988, Interpretation of the magnetotelluric impedance tensor, regional induction and local telluric distortion: J. Geophys., **62**, 119–127.

——— 1991, Geologic noise in magnetotelluric data: A classification of distortion type: Phys. Earth Plan. Int., **66**, 24–38.

Bailey, R. C., and Groom, R. W., 1987, Decomposition of the magnetotelluric impedence tensor which is useful in the presence of channeling: 57th Ann. Internat. Mtg., Soc. Expl. Geophys., Expanded Abstracts, 154–156.

Berdichevsky, M. N., and Dmitriev, V. I. 1976, Basic principles of interpretation of magnetotelluric curves, *in* Geolectric and geothermal studies: Adam, A., Ed., Akademini Kiado, 165–221.

Boerner, D. E., Kurtz, R. D., Craven, J. A., Rondenay, S., and Qian, W., 1995, A buried Proterozoic foredeep under the Western Canada Sedimentary Basin?: Geology, **23**, 297–300.

Borner, R. U., Oelsner, C., and Vygodner, K., 1999, Magnetotelluric investigations along the URSEIS profile: First results: Geologische Rundschau, **87**, 511–514.

Chakridi, R., Chouteau, M., and Mareschal, M., 1992, A simple technique for analysing and partly removing galvanic distortion from the magnetotelluric impedance tensor: Application to Abitibi and Kapuskasing data (Canada): Geophys. J. Internat., **108**, 917–929.

Chave, A. D., and Jones, A. G., 1997, Electric and magnetic field distortion decomposition of BC87 data: J. Geomagn. Geoelectr., **49**, 767–789.

Chave, A. D., and Smith, T. J., 1994, On electric and magnetic galvanic distortion tensor decompositions: J. Geophys. Res., **99**, 4669–4682.

Constable, S. C., Heinson, G. S., Anderson, G., and White, A., 1997, Seafloor electromagnetic measurements above Axial Seamount, Juan de Fuca Ridge: J. Geomagn. Geoelectr., **49**, 1327–1342.

Echternacht, F., Tauber, S., Eisel, M., Brasse, H., Schwarz, G., and Haak, V., 1997, Electromagnetic study of the active continental margin in northern Chile: Phys. Earth Plan. Int., **102**, 69–87.

Eisel, M., and Bahr, K., 1993, Electrical anisotropy in the lower crust of British Columbia: An interpretation of a magnetotelluric profile after tensor decomposition: J. Geomagn. Geoelectr., **45**, 1115–1126.

Groom, R. W., 1988, The effects of inhomogeneities on magnetotellurics: Ph.D. thesis, Univ. of Toronto.

Groom, R. W., and Bahr, K., 1992, Corrections for near surface effects: Decomposition of the magnetotelluric impedance tensor and scaling corrections for regional resistivities: A tutorial: Surv. Geophys., **13**, 341–380.

Groom, R. W., and Bailey, R. C., 1989, Decomposition of magnetotelluric impedance tensors in the presence of local three-dimensional galvanic distortion: J. Geophys. Res., **94**, 1913–1925.

——— 1991, Analytical investigations of the effects of near surface three-dimensional galvanic scatterers on MT tensor decomposition: Geophysics, **56**, 496–518.

Groom, R. W., Kurtz, R. D., Jones, A. G., and Boerner, D. E., 1993, A quantitative methodology for determining the dimensionality of conductivity structure and the extraction of regional impedance responses from magnetotelluric data: Geophys. J. Internat., **115**, 1095–1118.

Gupta, J. C., and Jones, A. G., 1995, Electrical conductivity structure of the Purcell anticlinorium in southeast British Columbia and northwest Montana: Can. J. Earth Sci., **32**, 1564–1583.

Habashy, T. M., Groom, R. W., and Spies, B. R., 1993, Beyond the Born and Rytov approximations: A nonlinear approach to electromagnetic scattering: J. Geophys. Res., **98**, 1759–1775.

Harinarayana, T., Hutton, V. R. S., and Jones, P. C., 1993, Lateral variations in conductivity structure across southern Scotland and northern England: Phys. Earth Plan. Int., **81**, 25–41.

Hoversten, G. M., 1996, Papua New Guinea MT: Looking where seismics is blind: Geophys. Prospect., **44**, 935–961.

Ingham, M., and Brown, C., 1998, A magnetotelluric study of the Alpine fault, New Zealand: Geophys. J. Internat., **135**, 542–552.

Jiracek, G. R., 1990, Near-surface and topographic distortion in electromagnetic induction: Surv. Geophys., **11**, 163–203.

Jones, A. G., 1988, Static shift of magnetotelluric data and its removal in a sedimentary basin environment: Geophysics, **53**, 967–978.

Jones, A. G., and Craven, J. A., 1990, The North American Central Plains conductivity anomaly and its correlation with gravity, magnetic, seismic and heat flow data in Saskatchewan: Phys. Earth Plan. Int., **60**, 169–194.

Jones, A. G., Craven, J. A., McNeice, G. A., Ferguson, I. J., Boyce, T., Farquarson, C., and Ellis, R. G., 1993b. The North American Central Plains conductivity anomaly within the Trans-Hudson orogen in northern Saskatchewan: Geology, **21**, 1027–1030.

Jones, A. G., and Dumas, I., 1993, Electromagnetic images of a volcanic zone: Phys. Earth Plan. Int., **81**, 289–314.

Jones, A. G., and Groom, R. G., 1993, Strike angle determination from the magnetotelluric impedance tensor in the presence of noise and local distortion: Rotate at your peril!: Geophys. J. Internat., **113**, 524–534.

Jones, A. G., Groom, R. W., and Kurtz, R. D., 1993a, Decomposition and modelling of the BC87 dataset: J. Geomagn. Geoelectr., **45**, 1127–1150.

Jones, A. G., and Schultz, A., 1997, Introduction to MT-DIW2 Special Issue: J. Geomagn. Geoelectr., **49**, 727–737.

Kawakami, N., Fujinawa, Y., Asch, T. H., and Takasugi, S., 1997, Local galvanic distortions in the central part of northeast Japan (Part 1): J. Geomagn. Geoelectr., **49**, 1387–1400.

Kurtz, R. D., Craven, J. A., Niblett, E. R., and Stevens, R. A., 1993, The conductivity of the crust and mantle beneath the Kapuskasing uplift: Electrical anisotropy in the upper mantle: Geophys. J. Internat., **113**, 483–498.

Larsen, J. C., 1977, Removal of local surface conductivity effects from low frequency mantle response curves: Acta Geodet. Geophys. Acad. Sci. Hung., **12**, 183–186.

Livelybrooks, D. W., Mareschal, M., Blais, E., and Smith, J. T., 1996, Magnetotelluric delineation of the Trillabelle massive sulfide body in Sudbury, Ontario: Geophysics, **61**, 971–986.

Marquis, G., Jones, A. G., and Hyndman, R. D., 1995, Coincident conductive and reflective lower crust across a thermal boundary in southern British Columbia, Canada: Geophys. J. Internat., **20**, 111–131.

Ogawa, Y., 1997, Two-dimensional inversion of Papua New Guinea magnetotelluric dataset assuming static shift as a Gaussian distribution: J. Geomagn. Geoelectrc., **49**, 857–867.

Ogawa, Y., Jones, A. G., Unsworth, M. J., Booker, J. R., Lu, X., Craven, J., Roberts, B., Parmelee, J., and Farquharson, C., 1996, Deep electrical conductivity structures of the Appalachian orogen in the southeastern U.S: Geophys. Res. Lett., **23**, 1597–1600.

Ogawa, Y., Nishida, Y., and Makino, M., 1994, A collision boundary imaged by magnetotellurics, Hidaka Mountains, central Hokkaido, Japan: J. Geophys. Res., **99**, 22373–22388.

Pous, J., Ledo, J., Marcuello, A., and Queralt, P., 1997, On the resolution of the Darai limestones by two-dimensional forward modeling: J. Geomagn. Geoelectr., **49**, 817–825.

Richards, M. L., Schmucker, U., and Steveling, E., 1982, Entzerrung der Impedanzkurven von magnetotellurischen Messungen in der Schwäbischen Alb, *in* Protokol über das Kolloquium "Elektromagnetische Tiefenforschung," 27–40.

Ritter, P., and Banks, R. J., 1998, Separation of local and regional information in distorted GDS response functions by hypothetical event analysis: Geophys. J. Internat., **135**, 923–942.

Sims, W. E., and Bostick, F. X., 1969, Methods of magnetotelluric analysis: Univ. of Texas Elec. Geophys. Res. Lab. Tech. Rpt. **58**.

Singer, B. Sh., 1992, Correction for distortions of magnetotelluric fields: Limits of validity of the static approach: Surv. Geophys., **13**, 309–340.

Smith, J. T., 1995, Understanding telluric distortion matrices: Geophys. J. Internat., **122**, 219–226.

——— 1997, Estimating galvanic-distortion magnetic fields in magnetotellurics: Geophys. J. Internat., **130**, 65–72.

Swift, C. M., 1967, A magnetotelluric investigation of an electrical conductivity anomaly in the south-western United States: Ph.D. thesis, Mass. Inst. Tachnology.

Toh, H., and Uyeshima, M., 1997, One-dimensional model study of the PNG dataset using site-independent Groom-Bailey decomposition: J. Geomagn. Geoelectr., **49**, 843–856.

Volti, T. K., 1999, Magnetotelluric measurements on the Methana Peninsula (Greece): Modelling and interpretation: Tectonophys., **301**, 111–132.

Wannamaker, P. E., Stodt, J. A., and Rijo, L., 1985, PW2D: Finite element program for solution of magnetotelluric responses of

two-dimensional earth resistivity structure: Earth Sci. Lab., Univ. Utah Res. Inst.
West, G., and Edwards, R. N., 1985, A simple parametric model for the electromagnetic response of an anomalous body in a host medium: Geophys., **50**, 2542–2557.
White, D. J., Jones, A. G., Lucas, S. B., and Hajnal, Z., 1999, Tectonic evolution of the Superior Boundary zone from coincident seismic reflection and magnetotelluric profiles: Tectonics, **18**, 430–451.
White, S. N., Chave, A. D., and Filloux, J. H., 1997, A look at galvanic distortion in the Tasman Sea and the Juan de Fuca plate: J. Geomagn. Geoelectr., **49**, 1373–1386.
Zhang, P., Perersen, L. B., Mareschal, M., and Chouteau, M., 1993, Channeling contribution to tipper vectors: A magnetic equivalent to electrical distortion: Geophys. J. Internat., **113**, 693–700.
Zhang, P., Roberts, R. G., and Pedersen, L. B., 1987, Magnetotelluric strike rules: Geophysics, **52**, 267–278.